The Journal of Chemical Physics

Analyzing the photoassociation spectrum of ultracold ^{85}Rb ^{133}Cs molecule in (3)$^3\Sigma^+$ state ⊘

Zi-wei Wang ⓘ ; Zi-ang Li; Xu-hui Bai ⓘ ; Ting Gong; Zhong-hua Ji ⓘ ; Yan-ting Zhao ⓘ ; Gao-ren Wang ✉ ⓘ

Check for updates

View Online   Export Citation

24 April 2024 12:26:35

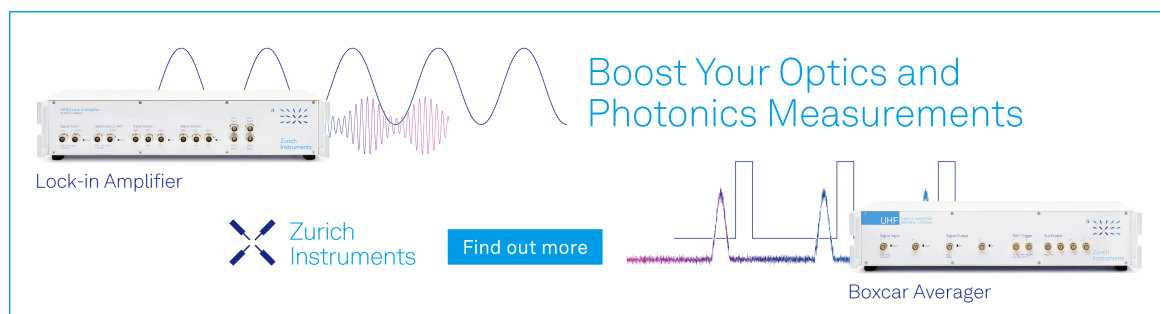# Analyzing the photoassociation spectrum of ultracold ^{85}Rb ^{133}Cs molecule in (3)$^3\Sigma^+$ state

Zi-wei Wang,[1,a] Zi-ang Li,[1] Xu-hui Bai,[1] Ting Gong,[2,b] Zhong-hua Ji,[2,3,c] Yan-ting Zhao,[2,3] and Gao-ren Wang[1,d]

AFFILIATIONS

[1] School of Physics, Dalian University of Technology, Dalian 116024, China
[2] State Key Laboratory of Quantum Optics and Quantum Optics Devices, Institute of Laser Spectroscopy, Shanxi University, Taiyuan 030006, China
[3] Collaborative Innovation Center of Extreme Optics, Shanxi University, Taiyuan 030006, China

[a] **Current address:** Department of Chemistry, Southern University of Science and Technology, Shenzhen 518055, China.
[b] **Current address:** School of Applied Science, Taiyuan University of Science and Technology, Taiyuan 030024, China.
[c] **Electronic mail:** jzh@sxu.edu.cn
[d] **Author to whom correspondence should be addressed:** gaoren.wang@dlut.edu.cn

ABSTRACT

We establish a theoretical model to analyze the photoassociative spectroscopy of ^{85}Rb ^{133}Cs molecules in the (3)$^3\Sigma^+$ state. The vibrational energy, spin–spin coupling constant, and hyperfine interaction constant of the (3)$^3\Sigma^+$ state are determined based on nine observed vibrational levels. Consequently, the Rydberg–Klein–Rees potential energy curve of the (3)$^3\Sigma^+$ state is obtained and compared with the *ab initial* potential energy curve. Our model can be adopted to analyze the photoassociative spectroscopy of other heteronuclear alkali-metal diatomic molecules in the (3)$^3\Sigma^+$ state.

Published under an exclusive license by AIP Publishing. https://doi.org/10.1063/5.0182907

I. INTRODUCTION

Photoassociation (PA) refers to the transition from the scattering state of two atoms to a molecular excited state by absorbing a photon.[1–3] PA spectroscopy in an ultracold atomic gas possesses a very high resolution and reveals properties of both the initial scattering state of the atom pair and the final molecular states,[4–8] which are essential for producing ultracold molecules.[9–12] PA spectroscopy is also used as a sophisticated detection technique to probe the electron–proton mass ratio variation,[13,14] the number of fluctuations in optical lattices,[15,16] and the pair correlations in many-body systems.[17,18] Recently, PA in ultracold atom–molecule or molecular gases is also studied.[19–24]

As cold Rb and Cs atoms were realized by laser cooling very early, studying the PA spectrum in an ultracold mixture of Rb and Cs atoms has a long history.[25–37] Since the initial state of PA is the scattering state of the atom pair, and a large portion of the scattering wave function lies in the long-range region, the Franck–Condon

(FC) factor between the initial scattering state and the weakly bound excited molecular state is expected to be relatively large. Hence, PA spectroscopy is first used to detect the molecular levels close to the dissociation threshold of the excited electronic states.[25] Some of the weakly bound levels are identified to belong to the (2)0$^+$ and (2)0$^-$ states [in Hund's case, (c) notation], which are studied in detail.[26–28] Later, it is shown that the deeply bound levels in the excited electronic states can also be detected by PA spectroscopy,[29] although the FC factor is expected to be small. These deeply bound levels in the excited electronic states can decay spontaneously to the ground vibrational levels in the ground electronic state.[30–32] This opens up a promising pathway to continuously produce ultracold ground state RbCs molecules via PA, followed by spontaneous decay. The deeply bound levels detected in Ref. 29 are identified to belong to the $\Omega = 0$ component of the (2)$^3\Pi$ state, where Ω is the projection of the total electronic angular momentum on the internuclear axis. Subsequently, the PA spectroscopy of this state is studied extensively.[30,33–36]

Recently, PA spectroscopy of RbCs molecules in the $(3)^3\Sigma^+$ state is performed, and several deeply bound vibrational levels, including the ground vibrational level of the $(3)^3\Sigma^+$ state, have been measured.[37] The PA spectrum of the $(3)^3\Sigma^+$ state has rich hyperfine structures. In contrast, no hyperfine structures are detected in the PA spectrum of the $\Omega = 0$ states[25,29] because of which the leading-order hyperfine splitting vanishes. Moreover, the $(3)^3\Sigma^+$ state is found to be an efficient pathway to produce absolutely ground state RbCs molecules.[37] For the observed PA spectrum in Ref. 37, the vibrational quantum numbers are assigned. However, the hyperfine structures of the PA spectrum are not studied.

In this work, we experimentally measure the PA spectrum of ^{85}Rb ^{133}Cs molecules in the $(3)^3\Sigma^+$ state and establish a theoretical model to analyze the observed spectrum. The hyperfine structures and the transition strength of the PA spectrum are modeled. The coupling strengths for the fine and hyperfine interactions of the nine observed vibrational levels of the $(3)^3\Sigma^+$ state are determined. In addition, we derive the Rydberg–Klein–Rees (RKR) potential energy curve of the $(3)^3\Sigma^+$ state based on the spectroscopic data obtained by our model.

This article is organized as follows: in Sec. II, the experimental setup to obtain the PA spectrum of RbCs molecules is described. In Sec. III, the theoretical model used in the analysis is introduced. In Sec. IV, the PA spectrum of ^{85}Rb ^{133}Cs molecule in the $(3)^3\Sigma^+$ state is analyzed with the model we presented. We summarize our work in Sec. V.

II. EXPERIMENTAL SETUP

Our experimental setup to obtain the PA spectrum of ^{85}Rb^{133}Cs molecules in the $(3)^3\Sigma^+$ state is the same as our previous publications,[27,35,36] in which the PA spectrum of other molecular states is studied. Given the completeness of the content, we will only give a brief explanation below.

In a vacuum chamber, 1×10^7 ^{85}Rb atoms in the $5S_{1/2}$ ($f = 2$) state with a density of 8×10^{10} cm^{-3} and 2×10^7 ^{133}Cs atoms in the $6S_{1/2}$ ($f = 3$) state with a density of 1.5×10^{11} cm^{-3} are produced using overlapped dark spontaneous force optical traps (dark-SPOT) with a space-adjustable optical layout.[38] The pressure is estimated to be 3×10^{-6} Pa, which is influenced by the atom resource in the vacuum chamber, and can be adjusted with the valve. Colliding atomic pairs of ^{85}Rb and ^{133}Cs are photoassociated into the $(3)^3\Sigma^+$ state, which is adiabatically correlated with the Rb($5P_{3/2}$) + Cs($6S_{1/2}$) dissociation limit at a long range. The produced accurate levels of the $(3)^3\Sigma^+$ state are dependent on the frequency of a tunable Ti:sapphire laser with a typical linewidth of 100 kHz and output power of up to around 1 W. The excited molecular levels are not stable and soon decay to the vibrational levels of the $X^1\Sigma^+$ state, including the lowest vibrational level. In the following $X^1\Sigma^+$ state, molecules are photoionized to molecule ions by a pulsed dye laser at a rate of 10 Hz through the $(2)^3\Pi_1$ state.[39] Finally, an electric field accelerates these photoionized ions to a pair of microchannel plates, followed by being amplified and recorded by a multichannel sampling with ten averages.

III. THEORETICAL MODEL

To analyze the PA spectrum, one needs to properly describe the initial and final states and the transition strength that are presented in the following.

A. Initial state

We refer to ^{133}Cs as atom 1 and ^{85}Rb as atom 2. The electron spin and nuclear spin quantum numbers of the ground state ^{133}Cs atom and ^{85}Rb atom are $s_1 = 1/2$, $I_1 = 7/2$ and $s_2 = 1/2$, $I_2 = 5/2$, respectively. The electron spin $\boldsymbol{s}_n$ and nuclear spin $\boldsymbol{I}_n$ of the same atom are coupled by hyperfine interaction to form the total angular momentum $\boldsymbol{f}_n$, where $n = 1, 2$. Experimentally, ^{133}Cs and ^{85}Rb atoms are initially prepared in the lowest hyperfine states, $f_1 = 3$ and $f_2 = 2$, respectively. The temperature of the atomic gas is around 100 μK, and s-wave scattering dominates at such an ultra-low temperature. Hence, the partial wave quantum number l equals zero. The initial scattering state of the atom pair can be described by the basis $|(s_1 I_1) f_1 (s_2 I_2) f_2 f l F\rangle$, where $\boldsymbol{f} = \boldsymbol{f}_1 + \boldsymbol{f}_2$, and $\boldsymbol{F} = \boldsymbol{f} + \boldsymbol{l}$. In the following, we refer to this basis as fragmentation basis. In the case considered in this work ($f_1 = 3$, $f_2 = 2$, and $l = 0$), $f = F = 1, 2, 3, 4,$ and 5. Initially, the states with different F are assumed to coexist incoherently. Since ultracold ^{133}Cs and ^{85}Rb atoms are unpolarized in the experiment, we assume that, for state with F, different m_F levels are equally populated incoherently, and the weight of the F state is $2F + 1$.

B. Excited molecular state

We adopt the following Hamiltonian to describe the molecules in the $(3)^3\Sigma^+$ state:

$$\hat{H} = \hat{H}_e + \hat{H}_v + \hat{H}_r + \hat{H}_{SS} + \hat{H}_{hf}, \tag{1}$$

where $\hat{H}_e$, $\hat{H}_v$, and $\hat{H}_r$ are the electronic, vibrational, and rotational Hamiltonian, respectively. The spin–spin interaction $\hat{H}_{SS}$ is given by[40]

$$\hat{H}_{SS} = \frac{2}{3}\lambda\left(3S_z^2 - \boldsymbol{S}^2\right), \tag{2}$$

where $\boldsymbol{S} = \boldsymbol{s}_1 + \boldsymbol{s}_2$ is the total electronic spin angular momentum and S_z is the component of $\boldsymbol{S}$ along the intermolecular axis. The hyperfine interaction $\hat{H}_{hf}$ includes two parts: the hyperfine interaction between the nuclear spin of ^{133}Cs atom and the electron spin is denoted by $\hat{H}_{hf}(1)$, and the hyperfine interaction related to the nuclear spin of ^{85}Rb atom is denoted by $\hat{H}_{hf}(2)$. $\hat{H}_{hf}(n)$ is given by[40]

$$\hat{H}_{hf}(n) = \sum_i (8\pi/3)\zeta(n)\boldsymbol{I}_n \cdot \boldsymbol{s}_i \delta(\boldsymbol{r}_{in}), \tag{3}$$

where $\zeta(n) = g g_{I_n} \mu_B \mu_N$. Here, g, g_{I_n}, μ_B, and μ_N are the g value for an electron, g value for the nucleus n, Bohr magneton, and nuclear magneton, respectively. In addition, $\boldsymbol{r}_{in}$ is the position vector of the electron i with respect to the nucleus n.

In the following, we adopt Hund's case (b) basis to obtain the matrix representation of $\hat{H}$. Conventionally, Hund's case (b) basis is expressed as $|\Lambda S v N J\rangle$, where Λ is the projection of the total electronic orbital angular momentum on the internuclear axis. For the

$(3)^3\Sigma^+$ state, Λ equals 0 and S is 1. Here, v is the vibrational quantum number. N results from the coupling between Λ and the rotational angular momentum R. Since Λ is zero for the $(3)^3\Sigma^+$ state, N is essentially the rotational angular momentum. As the initial state is the s-wave scattering state, the quantum number N is fixed to be 1 due to the transition selection rule. $J = N + S$ is the total angular momentum with the nuclear spin angular momentum excluded. In this work, we extend the conventional Hund's case (b) basis to include the nuclear spin angular momentum. The $(3)^3\Sigma^+$ state correlates with the Rb($5P$)+Cs($6S$) asymptote. Since the hyperfine splitting of Cs($6S$) is larger than that of Rb($5P$),[41] it is expected that for the RbCs molecules in the $(3)^3\Sigma^+$ state, the hyperfine interaction with Cs is larger than the hyperfine interaction with Rb. A similar situation has been observed for NaK.[42] As a result, the following coupling scheme is adopted: first, J is coupled with the nuclear spin angular momentum of ^{133}Cs I_1 to form F_1, and then, F_1 is coupled with the nuclear spin angular momentum of ^{85}Rb I_2 to form F. The full basis is expressed as $|\Lambda S v N J I_1 F_1 I_2 F\rangle$. Since we focus on the $(3)^3\Sigma^+$ state in this subsection, we will use the notation $|^3\Sigma^+ v N J I_1 F_1 I_2 F\rangle$. The matrix elements of different terms in Eq. (1) are given in Appendix A.

The total angular momentum F is a good quantum number. The molecular states with $F = 0, 1, 2, 3, 4, 5, 6$ can be excited from the initial scattering state due to the transition selection rule.

C. Line strength

To characterize the transition probability between the initial scattering state and the final excited molecular state, we calculate the line strength, which is the square of the transition dipole moment. In the following, we first expand the fragmentation basis in Hund's case (b) basis and then present the expression of the transition dipole moment in Hund's case (b) basis.

Since the two atoms are in the ground state initially, the total electronic orbital angular momentum L and its projection on the internuclear axis Λ are equal to 0. As a result, N in Hund's case (b) basis is identical to the partial-wave quantum number l in the fragmentation basis. Since the s-wave scattering state is considered, N is 0. Furthermore, J is the same with S due to $N = 0$. Under such circumstances, the fragmentation basis can be expressed by Hund's case (b) basis as

$$
\begin{aligned}
|(s_1 I_1) f_1 (s_2 I_2) f_2 \, f \, I F\rangle &= \sum_{S I J F_1} (-1)^{l+S+J+I_1+I_2+I+2F} \\
&\quad \times \left[(2f_1+1)(2f_2+1)(2f+1)(2S+1) \right. \\
&\quad \left. \times (2J+1)(2F_1+1) \right]^{1/2} (2I+1) \\
&\quad \times \begin{Bmatrix} N & S & J \\ I & F & f \end{Bmatrix} \begin{Bmatrix} J & I_1 & F_1 \\ I_2 & F & I \end{Bmatrix} \\
&\quad \times \begin{Bmatrix} s_1 & I_1 & f_1 \\ s_2 & I_2 & f_2 \\ S & I & f \end{Bmatrix} |\Lambda S N J I_1 F_1 I_2 F\rangle,
\end{aligned} \tag{4}
$$

where $I = i_1 + i_2$ is the total nuclear spin angular momentum and the two-row and three-row arrays in the curly bracket are Wigner $6j$ and $9j$ symbols, respectively.

The expression of the transition dipole moment in Hund's case (b) basis, excluding the nuclear spin, is derived in Ref. 43. In the Hund's case (b) basis adopted in this work, the expression of the transition moment is modified to be

$$
\begin{aligned}
&\langle \Lambda S N J I_1 F_1 I_2 F | d | \Lambda' S' N' J' I_1 F_1' I_2 F'\rangle \\
&= \delta_{SS'} (-1)^p \big[(2F+1)(2F'+1)(2F_1+1)(2F_1'+1) \\
&\quad \times (2J+1)(2J'+1)(2N+1)(2N'+1) \big]^{\frac{1}{2}} \\
&\quad \times \begin{pmatrix} N & 1 & N' \\ -\Lambda & \Lambda'-\Lambda & \Lambda' \end{pmatrix} \begin{Bmatrix} N & 1 & N' \\ J' & S & J \end{Bmatrix} \begin{Bmatrix} J & I_1 & F_1 \\ F_1' & 1 & J' \end{Bmatrix} \\
&\quad \times \begin{Bmatrix} F_1 & I_2 & F \\ F' & 1 & F_1' \end{Bmatrix} M_{\Lambda-\Lambda'},
\end{aligned} \tag{5}
$$

where $p = F' + F_1 + F_1' + J + J' + I_1 + I_2 + S + 1 - \Lambda$, $M_{\Lambda-\Lambda'} = \langle \Lambda | d_{\Lambda-\Lambda'} | \Lambda' \rangle$, and d_λ is the $\lambda = 0, \pm 1$ component of the transition dipole moment d. As stated above, both Λ and Λ' for the levels before and after the PA transition considered in this work are 0. Therefore, the M_0 component is relevant in our calculation. Furthermore, we assume that M_0 is constant in this work. Since the relative transition probability is considered, the value of M_0 is set to be 1. In Eq. (5), the array in the parentheses is the Wigner $3j$ symbol.

IV. RESULTS AND DISCUSSION

Before analyzing the experimental spectrum, the influences of the interactions of $\hat{H}_{SS}$, $\hat{H}_{hf}(1)$, and $\hat{H}_{hf}(2)$ on the splitting of a rovibrational level are shown in Fig. 1. The $N = 1$ rotational level without interactions of $\hat{H}_{SS}$, $\hat{H}_{hf}(1)$, and $\hat{H}_{hf}(2)$ is shown in Fig. 1(a). The vibrational energy E_v is set to be zero in the calculation. When the spin–spin interaction of $\hat{H}_{SS}$ is turned on, the $N = 1$ rotational level of the $(3)^3\Sigma$ electronic state splits into three levels, labeled by $J = 0, 1, 2$. The energy level determined by $\hat{H}_r$ and $\hat{H}_{SS}$ can be calculated as follows:[44]

$$
\begin{aligned}
E_{N,J=N+1} &= B_v N(N+1) + (2N+3)B_v - \frac{1}{3}\lambda_v \\
&\quad - \sqrt{(2N+3)^2 B_v^2 + \lambda_v^2 - 2\lambda_v B_v}, \\
E_{N,J=N} &= B_v N(N+1) + \frac{2}{3}\lambda_v, \\
E_{N,J=N-1} &= B_v N(N+1) - (2N-1)B_v - \frac{1}{3}\lambda_v \\
&\quad + \sqrt{(2N-1)^2 B_v^2 + \lambda_v^2 - 2\lambda_v B_v}.
\end{aligned} \tag{6}
$$

For molecules consisting of heavy atoms, such as Rb$_2$ and Cs$_2$, $|\lambda_v|$ is much larger than B_v.[45,46] The same situation is expected for RbCs molecules. In addition, λ_v can be positive[46] or negative.[44] In Fig. 1(b), the results with positive (red dashed lines) and negative (black solid lines) λ_v are shown. For $\lambda_v > 0$ and $\lambda_v / B_v \gg 1$, the three levels, energetically from low to high, are $J = 2$, $J = 0$, and $J = 1$. Moreover, the energy spacing between the $J = 2$ level and $J = 0$ level, which is on the order of λ_v, is larger than the energy spacing between the $J = 0$ level and $J = 1$ level, which is on the order of B_v. For $\lambda_v < 0$ and $|\lambda_v| / B_v \gg 1$, the three levels in increasing order of energies are
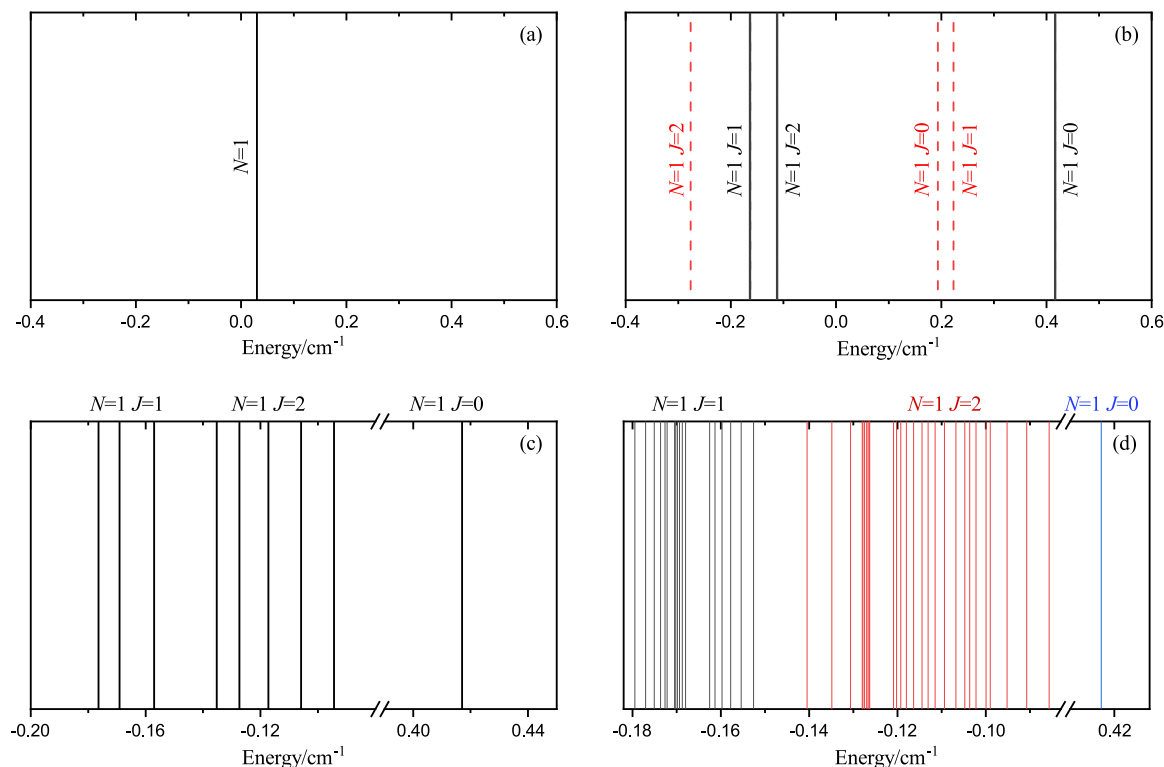
FIG. 1. (a) The $N = 1$ rotational level without electronic spin–spin interaction $\hat{H}_{SS}$ and hyperfine interactions $\hat{H}_{hf}(1)$ and $\hat{H}_{hf}(2)$. (b) The energy level splitting when $\hat{H}_{SS}$ is included. The results with positive (red dashed line) and negative (black solid line) electronic spin–spin interaction parameter λ_v are shown. (c) The energy level splitting when $\hat{H}_{SS}$ and $\hat{H}_{hf}(1)$ are included. (d) The energy level splitting when $\hat{H}_{SS}$, $\hat{H}_{hf}(1)$, and $\hat{H}_{hf}(2)$ are included. In the calculation, the vibrational energy E_v is set to be zero. $B_v = 0.014\,96$ cm^{-1}, $|\lambda_v| = 0.29$ cm^{-1}, $K_1 = 0.0051$ cm^{-1}, and $K_2 = 0.0035$ cm^{-1} are adopted, which are related to the $v = 8$ vibrational level of the $(3)^3\Sigma^+$ state. In the calculation of (c) and (d), negative λ_v is used.

$J = 1$, $J = 2$, and $J = 0$. The energy spacing between the $J = 1$ and $J = 2$ levels is on the order of B_v and that between the $J = 2$ and $J = 0$ levels is on the order of λ_v. In the following, we will show that λ_v is deduced to be negative for the vibrational levels observed via the PA spectrum. As shown in Fig. 1(c), the $J = 1, 2$ levels further split when $\hat{H}_{hf}(1)$ is also turned on. Since $I_1 = 7/2$, the $J = 1$ level splits into three levels with $F_1 = 5/2, 7/2, 9/2$. The $J = 2$ level splits into five levels with $F_1 = 3/2, 5/2, 7/2, 9/2, 11/2$. In contrast, the $J = 0$ level does not split. When $\hat{H}_{hf}(2)$ is considered, the levels stemmed from $J = 1, 2$ levels further split, as shown in Fig. 1(d). Meanwhile, the $J = 0$ level still does not split. Due to the selection rules, not all the hyperfine levels shown in Fig. 1(d) can be populated via PA transition from the initial scattering state.

Now, we analyze the PA spectra observed experimentally. The vibrational levels $v = 0$–$5, 7$–10 of the $(3)^3\Sigma^+$ state are detected via PA spectroscopy. The $v = 6$ level is not detected via PA spectroscopy, which is probably due to tiny the Franck–Condon overlap integral between the $v = 6$ state and the initial scattering state. It should be noted that starting from the $v = 0$ level of the ground electronic state, the $v = 6$ level of $(3)^3\Sigma^+$ state is observed by mass-resolved resonance enhanced two-photon ionization.[48] The PA spectra of nine vibrational levels with $v = 0$–$2, 4, 5, 7$–10 show a similar pattern and are

analyzed in this work. The PA spectra of the $v = 3$ level show anomalous structures and is left for future study. The potential energy curves of the $(3)^3\Sigma^+$ state and the neighboring $(2)^1\Pi$ and $(2)^3\Pi$ states from Ref. 47 are shown in Fig. 2. The energy range studied in the current work is indicated by the shadowed area in Fig. 2.

As an illustration, the PA spectra observed experimentally for $v = 8$ are shown in red lines in Fig. 3. The threshold energy of the initial scattering channel ^{133}Cs$(6S)|f_1 = 3\rangle + {}^{85}Rb(5S)|f_2 = 2\rangle$ is set to be zero. The energy of the PA transition shown in Fig. 3 is determined by adding the energy shift indicated in the horizontal axis and E_0 labeled in the plot. Two groups of spectrum peaks are clearly observed. In each group, abundant hyperfine structures are observed. This indicates that the two groups are related to the $J = 1, 2$ levels. The energy spacing between the centers of the two groups is roughly 0.06 cm^{-1} and is on the same order as the rotational constants calculated with the *ab initio* potential in Ref. 49, which are presented in Table I. Based on these observations, we deduced that λ_v is negative. The first group of spectrum peaks stems from the $J = 1$ level. As shown in Fig. 1(c), the $J = 1$ level splits into three levels by $\hat{H}_{hf}(1)$. Figure 3 clearly shows that the first group of spectrum peaks has three subgroups. The hyperfine structures in each subgroup are due to $\hat{H}_{hf}(2)$. The second group of spectrum peaks stems from the
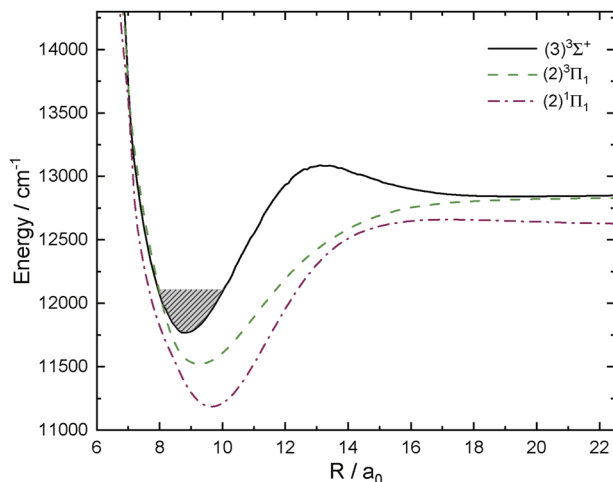
FIG. 2. The potential energy curve of the $(3)^3\Sigma^+$ state (black solid line). The energy region detected by PA spectroscopy is indicated by the shadowed area. The potential energy curves of neighboring $(2)^3\Pi$ (green dashed line) and $(2)^1\Pi$ (purple dotted-dashed line) states. The potential energy curves are adopted from Ref. 47.
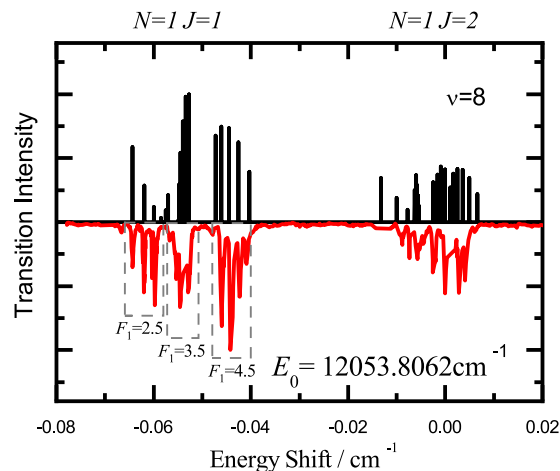

FIG. 3. Observed (red line) and calculated (black line) PA spectrum of the vibrational level $v = 8$. The observed and calculated PA spectra are normalized, respectively. The energy of the strongest peak in the second group of peaks is shifted to be zero. The shifted energy E_0 is labeled in the plot.

$J = 2$ level. As shown in Fig. 1(c), the $J = 2$ level splits into five levels by $\hat{H}_{hf}(1)$, among which, the $F_1 = 11/2$ level cannot be populated. The remaining four levels, labeled by $F_1 = 3/2, 5/2, 7/2$ and $9/2$, are further split by $\hat{H}_{hf}(2)$ and overlap with each other.

To reproduce the observed spectra, the rotational constants B_v are fixed to be the theoretically calculated values presented in Table I since we cannot determine B_v and λ_v simultaneously with the available experimental data. The spin–spin coupling constant λ_v, the hyperfine interaction constants K_1 and K_2, and the vibrational energy E_v are treated as fitting parameters. The initial value of λ_v, K_1, K_2, and E_v are estimated as follows: first, we read out the energy spacing between the centers of the two groups of peaks associated with $J = 1$ and $J = 2$, from which we estimate λ_v according to Eq. (6). Next, we read out the centers of the three subgroups in the $J = 1$ ground, from which we estimate K_1 according to Eqs. (A4) and (A5). Furthermore, we read out the spread of each subgroup associated with $J = 1$, from which we estimate K_2 according to Eq. (A6). Finally, E_v is estimated by setting the calculated energy position of the center of the $J = 1$ group to be the experimentally observed value.

For the hyperfine levels, which can be populated via photoassociation transition, the corresponding signal may not be identified in the experimentally observed PA spectra due to the following reasons: the photoassociation transition probability may be small, and the signal is masked by background noise. For levels with small energy intervals, the corresponding peaks in the PA spectrum may overlap due to broadening or may be indistinguishable due to the finite resolution of the PA laser, which is 60 MHz in our experiments. To fit λ_v, K_1, K_2, and E_v, the notable peaks in the experimentally observed PA spectra, which are well isolated from the background noise, are identified. The laser frequencies at which the notable peaks have maxima are set to be the center frequencies of the peaks and are listed in the supplementary material. The hyperfine levels in the theoretical calculation that are closest to the center frequencies of notable peaks are selected. The four parameters are tuned to minimize the sum of the differences between the center frequencies of the experimental peaks and the closest theoretical levels.

The fitted spectra are shown in black lines in Fig. 3. Similar calculations are performed for all the other eight vibrational levels. The results are shown in Fig. 5 in Appendix B. As described in Sec. II,

TABLE I. Fitted vibrational energy E_v, electronic spin–spin interaction parameters λ_v, and hyperfine interaction parameters K_1 and K_2 for the $v = 0$–2, 4, 5, 7–10 vibrational levels of ^{85}Rb ^{133}Cs molecules in the $(3)^3\Sigma^+$ state are summarized. The rotation constants B_v calculated with the *ab initio* potential given in Ref. 49 are also listed.

v	0	1	2	4	5	7	8	9	10
E_v (cm^{-1})	11 780.28	11 809.66	11 841.31	11 924.40	11 960.21	12 018.60	12 053.92	12 085.68	12 113.35
B_v (cm^{-1})	0.015 29	0.015 26	0.015 23	0.015 15	0.015 11	0.0150	0.014 96	0.0149	0.014 84
λ_v (cm^{-1})	−0.55	−0.45	−0.75	−0.95	−0.5	−0.29	−0.29	−0.3	−0.22
K_1 (cm^{-1})	0.005	0.003 5	0.006	0.004 755	0.005	0.004	0.005 1	0.0042	0.003 5
K_2 (cm^{-1})	0.002 5	0.001 5	0.002	0.002	0.002 5	0.0035	0.003 5	0.002	0.002

to observe the PA spectra experimentally, the PA process is followed by spontaneous decay and photoionization processes. In the current work, we calculate the line strength of the PA process and do not simulate the spontaneous decay and photoionization processes. As a result, one cannot directly compare the calculated line strength and the height of the experimental peaks. Nevertheless, it is useful to calculate the line strength of the PA process. The transition dipole moment between some of the hyperfine levels of the $(3)^3\Sigma^+$ state and the initial scattering state is zero. These hyperfine levels can be identified by calculating the line strength and are excluded in the fitting of the experimental spectrum. Moreover, if the line strength of the PA process is large, the corresponding peak in the PA spectra is probably high, as shown in Figs. 3 and 5.

The values of the fitting parameters for the nine levels are listed in Table I. As expected, $|\lambda|$ is one order of magnitude larger than B_v. The electronic spin–spin interaction splits the $(3)^3\Sigma^+$ state into $(3)^3\Sigma_0^+$ and $(3)^3\Sigma_{\pm1}^+$, and λ is equal to half of the energy difference between the $(3)^3\Sigma_{\pm1}^+$ and $(3)^3\Sigma_0^+$ states.[50] The electronic transition energies T_e from the minimum of the ground electronic state are calculated in Ref. 47 to be 15 627 and 15 611 cm^{-1} for the $(3)^3\Sigma_0^+$ and $(3)^3\Sigma_{\pm1}^+$ states, respectively, which implies that $\lambda = -8$ cm^{-1}. Meanwhile, T_e is calculated to be 16 099 cm^{-1} for both the $(3)^3\Sigma_0^+$ and $(3)^3\Sigma_{\pm1}^+$ states in Ref. 49, which implies that $\lambda = 0$. Our fitting values of λ_v for the nine vibrational levels listed in Table I are in between the values determined by these two *ab initio* calculations.

The hyperfine interaction parameters of molecules in the ground electronic state have been calculated via the *ab initio* method,[51–55] which accurately described the experimentally observed hyperfine levels.[56–58] Recently, the hyperfine structures of the $(1)^3\Pi_1$ state have been studied by fitting spectroscopy.[59] To our best knowledge, there are no *ab initio* calculations for RbCs molecules in the excited electronic state, and such calculations are outside the scope of the current work.

All the fitted vibrational energy E_v listed in Table I are smaller than the corresponding values E_v^{cal} calculated with the *ab initio* potential obtained in Ref. 49. By shifting the *ab initio* potential 306.92 cm^{-1} downward, the summation of the absolute difference between the calculated and fitted vibrational energy $|E_v - E_v^{cal}|$ is minimal. In such case, the absolute differences $|E_v - E_v^{cal}|$ are shown in Fig. 4(a) by the black-filled bars, which are still considerably large, except for $v = 2$. Based on the fitted vibrational energy, E_v, and the calculated rotational constant, B_v, listed in Table I, we construct the RKR potential of the $(3)^3\Sigma^+$ state using the algorithm given in Ref. 60. The obtained RKR potential is represented by the red dotted-dashed line shown in Fig. 4(b). The *ab initio* potential obtained in Ref. 49 is also represented by the black solid line shown in Fig. 4(b). The agreement between the vibrational energies calculated with the RKR potential and the fitted values is improved as indicated by the red hollow bars shown in Fig. 4(a). It is noted that the vibrational levels of the $(3)^3\Sigma^+$ state are observed by mass-resolved resonance enhanced two-photon ionization,[48] and the fitted vibrational energies E_v in our work agree with the values obtained in Ref. 48.

In this work, we do not consider the coupling between the $(3)^3\Sigma^+$ state with other electronic states. As shown in Fig. 2, there are $(2)^1\Pi$ and $(2)^3\Pi$ states in the neighborhood of the $(3)^3\Sigma^+$ state, which are coupled by the spin–orbit interaction. In the energy range studied in this work, the vibrational levels of the $(2)^1\Pi$ and
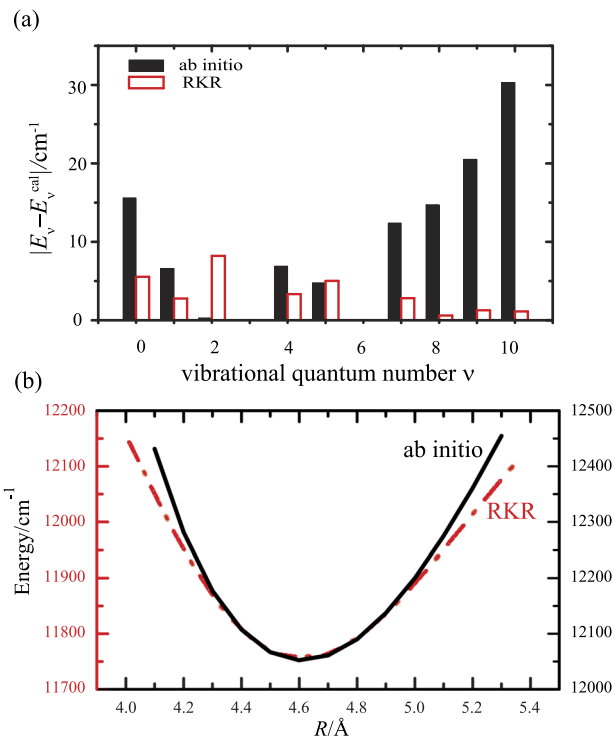

FIG. 4. (a) The absolute difference between the calculated vibrational energy E_v^{cal} and the fitted one E_v. Black solid bar: E_v^{cal} is calculated with the potential energy curve of the $(3)^3\Sigma$ state calculated by using the *ab initio* method in Ref. 49; red hollow bar: E_v^{cal} is calculated with the potential energy curve calculated by using the RKR method in our work. The corresponding potential energy curves are shown in (b).

$(2)^3\Pi$ states were observed.[37,48] Currently, there are no depertubation analysis of the $(3)^3\Sigma^+$-$(2)^1\Pi$-$(2)^3\Pi$ system in the literature. We examined the energies of the vibrational levels of these three electronic states and found that the levels of the $(3)^3\Sigma^+$ and $(2)^1\Pi$ states are more close to each other. It is inferred that the $(3)^3\Sigma^+$ state is more perturbed by the $(2)^1\Pi$ state. Since there is no hyperfine splitting in the $(2)^1\Pi$ state,[61] the coupling between the $(3)^3\Sigma^+$ state and the $(2)^1\Pi$ state only compresses the energy splitting of the hyperfine structures of the $(3)^3\Sigma^+$ state. This implies that the Hamiltonian given in Eq. (1) is an effective one, and the hyperfine interaction parameters of the $(3)^3\Sigma^+$ state may be underestimated in our model.

V. CONCLUSIONS

We theoretically analyze the photoassociation (PA) spectrum of the $(3)^3\Sigma^+$ state of the ^{85}Rb ^{133}Cs molecule. The vibrational energy, electronic spin–spin parameter, and hyperfine interaction constant of vibrational levels $v = 0$–2, 4–5, 7–10 are determined by fitting the PA spectrum. Based on the fitted vibrational energy and the calculated rotational constant, we constructed the RKR potential curve of the $(3)^3\Sigma^+$ state.

24 April 2024 12:26:35

The PA spectrum of $v = 3$ vibrational level has also been probed experimentally, the pattern of which is different from those of the vibrational levels considered in this work. As pointed out in Ref. [37], this is probably due to the fact that there is a vibrational level of the $(2)^3\Pi_{0^-}$ state very close to the $v = 3$ vibrational level, and the coupling between these levels results in a particular pattern of the PA spectrum. In the future, we will expand the current model to include the $(2)^3\Pi_{0^-}$ state and analyze the PA spectrum of $v = 3$ level.

SUPPLEMENTARY MATERIAL

In the supplementary material, the selected peaks of the PA spectrum used in the fitting are marked, and the center frequencies of these selected peaks are listed.

ACKNOWLEDGMENTS

AUTHOR DECLARATIONS

Conflict of Interest

The authors have no conflicts to disclose.

Author Contributions

Zi-wei Wang: Conceptualization (equal); Investigation (equal); Writing – original draft (equal); Writing – review & editing (equal). **Zi-ang Li**: Conceptualization (supporting); Investigation (supporting); Writing – original draft (supporting); Writing – review & editing (supporting). **Xu-hui Bai**: Conceptualization (supporting); Investigation (supporting); Writing – original draft (supporting); Writing – review & editing (supporting). **Ting Gong**: Conceptualization (equal); Investigation (equal); Writing – original draft (supporting); Writing – review & editing (supporting). **Zhong-hua Ji**: Conceptualization (equal); Funding acquisition (equal); Investigation (equal); Supervision (equal); Writing – original draft (equal); Writing – review & editing (equal). **Yan-ting Zhao**: Funding acquisition (equal); Supervision (equal); Writing – original draft (equal); Writing – review & editing (equal). **Gao-ren Wang**: Conceptualization (equal); Funding acquisition (equal); Investigation (equal); Supervision (equal); Writing – original draft (equal); Writing – review & editing (equal).

DATA AVAILABILITY

The data that support the findings of this study are available from the corresponding author upon reasonable request.

APPENDIX A: THE MATRIX ELEMENTS OF THE HAMILTONIAN OPERATORS

The first three terms in, $\hat{H}_e + \hat{H}_v + \hat{H}_r$ is the diagonal matrix in Hund's case (b) basis, and the diagonal matrix element is given by

$$\langle {}^3\Sigma^+ vNJ|\hat{H}_e + \hat{H}_v + \hat{H}_r|{}^3\Sigma^+ vNJ\rangle = E_v + B_v N(N+1), \quad \text{(A1)}$$

where E_v and B_v are the energy and rotational constant of the vibrational level v, respectively. The diagonal matrix elements of spin–spin interaction $\hat{H}_{SS}$ are as follows:[42,62]

$$\langle {}^3\Sigma^+ vNJ|\hat{H}_{SS}|{}^3\Sigma^+ vNJ\rangle = \begin{cases} -\dfrac{N+1}{2N-1} \times \dfrac{2}{3}\lambda_v, & J = N-1, \\ \dfrac{2}{3}\lambda_v, & J = N, \\ -\dfrac{N-1}{2N+3} \times \dfrac{2}{3}\lambda_v, & J = N+1, \end{cases} \quad \text{(A2)}$$

where λ_v represents the spin–spin coupling constant of the vibrational level v. The nonvanishing off-diagonal matrix elements are expressed by[42,62]

$$\langle {}^3\Sigma^+ vNJ|\hat{H}_{SS}|{}^3\Sigma^+ vN'J\rangle = \frac{3\sqrt{(N+1)(N+2)}}{2N+3} \times \frac{2}{3}\lambda_v,$$
$$N' = N+2, \quad J = N+1. \quad \text{(A3)}$$

The diagonal matrix elements of hyperfine interaction $\hat{H}_{hf}(1)$ are given by[63]

$$\langle {}^3\Sigma^+ vNJI_1F_1I_2F|\hat{H}_{hf}(1)|{}^3\Sigma^+ vNJI_1F_1I_2F\rangle$$
$$= \begin{cases} -K_1 G(F_1, N-1, I_1)/N, & J = N-1, \\ K_1 G(F_1, N, I_1)/N(N+1), & J = N, \\ K_1 G(F_1, N+1, I_1)/(N+1), & J = N+1, \end{cases} \quad \text{(A4)}$$

where $K_1 = (8\pi/3)\zeta(1)\langle {}^3\Sigma^+ v\|\sum_i \mathbf{s}_i \delta(\mathbf{r}_{i1})\|{}^3\Sigma^+ v\rangle$ is the hyperfine interaction constant characterizing the strength of $\hat{H}_{hf}(1)$ and $G(F, N, I) = [F(F+1) - N(N+1) - I(I+1)]/2$. The nonvanishing off-diagonal matrix elements of $\hat{H}_{hf}(1)$ are[63]

$$\langle {}^3\Sigma^+ vNJI_1F_1I_2F|\hat{H}_{hf}(1)|{}^3\Sigma^+ vNJ'I_1F_1I_2F\rangle$$
$$= \begin{cases} -K_1 \dfrac{1}{2N}\left(\dfrac{N+1}{2N+1}\right)^{1/2}[(F_1+N+I_1+1)(N+I_1-F_1) \\ \quad \times (F_1+N-I_1)(F_1+I_1+1-N)]^{1/2}, & J = N, \quad J' = N-1, \\ -K_1 \dfrac{1}{2(N+1)}\left(\dfrac{N}{2N+1}\right)^{1/2}[(F_1+N+I_1+2)(N+I_1+1-F_1) \\ \quad \times (F_1+N+1-I_1)(F_1+I_1-N)]^{1/2}, & J = N, \quad J' = N+1. \end{cases}$$
$$\text{(A5)}$$

The diagonal matrix elements of $\hat{H}_{hf}(2)$ are expressed as[63]

$$\langle {}^3\Sigma^+ vNJI_1F_1I_2F|\hat{H}_{hf}(2)|{}^3\Sigma^+ vNJI_1F_1I_2F\rangle$$
$$= \begin{cases} K_2 G(I_1, F_1, N-1)G(F, F_1, I_2)/[NF_1(F_1+1)], & J = N-1, \\ -K_2 G(I_1, F_1, N)G(F, F_1, I_2)/[N(N+1)F_1(F_1+1)], & J = N, \\ -K_2 G(I_1, F_1, N+1)G(F, F_1, I_2)/[(N+1)F_1(F_1+1)], & J = N+1, \end{cases}$$
$$\text{(A6)}$$

24 April 2024 12:26:35

where $K_2 = (8\pi/3)\zeta(2)\langle^3\Sigma^+ v\|\sum_i \boldsymbol{s}_i\delta(\boldsymbol{r}_{i2})\|^3\Sigma^+ v\rangle$ is the hyperfine interaction constant, characterizing the strength of $\hat{H}_{hf}(2)$. Since $\hat{H}_{hf}(2)$ is weak, the off-diagonal matrix elements of $\hat{H}_{hf}(2)$ are neglected.

APPENDIX B: THE PA SPECTRA OF $v = 0$–2, 4–5, 7, 9, 10 VIBRATIONAL LEVELS

The PA spectra of vibrational levels $v = 0$–2, 4, 5, 7, 9, 10 are shown in Fig. 5.
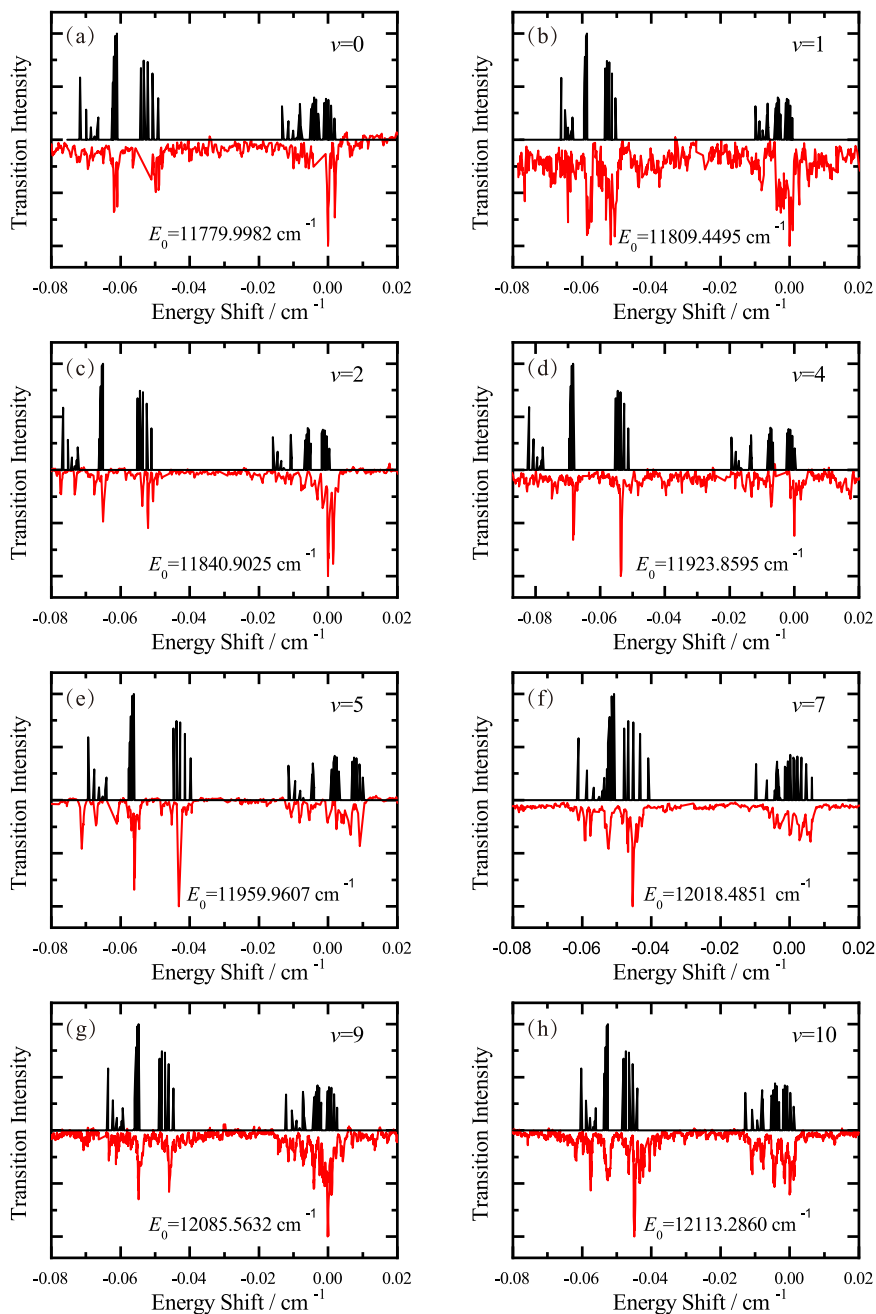

FIG. 5. Observed (red line) and calculated (black line) PA spectra of vibrational levels $v = 0$ (a), $v = 1$ (b), $v = 2$ (c), $v = 4$ (d), $v = 5$ (e), $v = 7$ (f), $v = 9$ (g), and $v = 10$ (h). For each vibrational level, the observed and calculated PA spectra are normalized, respectively. The energy of the strongest peak in the second group of peaks is shifted to be zero. The shifted energy E_0 is labeled in each subplot.

REFERENCES

[1] K. M. Jones, E. Tiesinga, P. D. Lett, and P. S. Julienne, Rev. Mod. Phys. **78**, 483 (2006).

[2] C. P. Koch and M. Shapiro, Chem. Rev. **112**, 4928 (2012).

[3] J. Ulmanis, J. Deiglmayr, M. Repp, R. Wester, and M. Weidemüller, Chem. Rev. **112**, 4890 (2012).

[4] K. Enomoto, R. Takabatake, T. Suzuki, Y. Takasu, Y. Takahashi, and M. Baba, Phys. Rev. A **104**, 013118 (2021).

[5] S. S. Kale, Y. P. Chen, and S. Kais, J. Chem. Theory Comput. **17**, 7822 (2021).

[6] W. Liu, N. Zheng, V. Sovkov, J. Xu, Y. Li, Y. Fu, P. Li, J. Wu, J. Ma, L. Xiao, and S. Jia, Phys. Chem. Chem. Phys. **24**, 15135 (2022).

[7] T. Franzen, B. Pollklesener, C. Sillus, and A. Görlitz, Phys. Rev. A **107**, 023114 (2023).

[8] L. R. B. Picard, J. T. Zhang, W. B. Cairncross, K. Wang, G. E. Patenotte, A. J. Park, Y. Yu, L. R. Liu, J. D. Hood, R. González-Férez, and K.-K. Ni, Phys. Rev. Res. **5**, 023149 (2023).

[9] G. Quéméner and P. S. Julienne, Chem. Rev. **112**, 4949 (2012).

[10] Y. Yu, K. Wang, J. D. Hood, L. R. B. Picard, J. T. Zhang, W. B. Cairncross, J. M. Hutson, R. Gonzalez-Ferez, T. Rosenband, and K.-K. Ni, Phys. Rev. X **11**, 031061 (2021).

[11] D. Mitra, K. H. Leung, and T. Zelevinsky, Phys. Rev. A **105**, 040101 (2022).

[12] I. Stevenson, A. Z. Lam, N. Bigagli, C. Warner, W. Yuan, S. Zhang, and S. Will, Phys. Rev. Lett. **130**, 113002 (2023).

[13] M. Gacesa and R. Côté, J. Mol. Spectrosc. **300**, 124 (2014).

[14] M. S. Safronova, D. Budker, D. DeMille, D. F. J. Kimball, A. Derevianko, and C. W. Clark, Rev. Mod. Phys. **90**, 025008 (2018).

[15] B. Yang, H. Sun, C.-J. Huang, H.-Y. Wang, Y. Deng, H.-N. Dai, Z.-S. Yuan, and J.-W. Pan, Science **369**, 550 (2020).

[16] Z.-Y. Zhou, G.-X. Su, J. C. Halimeh, R. Ott, H. Sun, P. Hauke, B. Yang, Z.-S. Yuan, J. Berges, and J.-W. Pan, Science **377**, 311 (2022).

[17] H. Konishi, K. Roux, V. Helson, and J.-P. Brantut, Nature **596**, 509 (2021).

[18] M. Weyland, S. S. Szigeti, R. A. B. Hobbs, P. Ruksasakchai, L. Sanchez, and M. F. Andersen, Phys. Rev. Lett. **126**, 083401 (2021).

[19] J. Pérez-Ríos, M. Lepers, and O. Dulieu, Phys. Rev. Lett. **115**, 073201 (2015).

[20] M. Gacesa, J. N. Byrd, J. Smucker, J. A. Montgomery, and R. Côté, Phys. Rev. Res. **3**, 023163 (2021).

[21] J. Schnabel, T. Kampschulte, S. Rupp, J. Hecker Denschlag, and A. Köhn, Phys. Rev. A **103**, 022820 (2021).

[22] A. A. Elkamshishy and C. H. Greene, J. Phys. Chem. A **127**, 18 (2023).

[23] B. Shammout, L. Karpa, S. Ospelkaus, E. Tiemann, and O. Dulieu, J. Phys. Chem. A **127**, 7872 (2023).

[24] J. Cao, B.-Y. Wang, H. Yang, Z.-J. Fan, Z. Su, J. Rui, B. Zhao, and J.-W. Pan, Phys. Rev. Lett. **132**, 093403 (2024).

[25] A. J. Kerman, J. M. Sage, S. Sainis, T. Bergeman, and D. DeMille, Phys. Rev. Lett. **92**, 033004 (2004).

[26] Z.-H. Ji, H.-S. Zhang, J.-Z. Wu, J.-P. Yuan, Y.-T. Zhao, J. Ma, L.-R. Wang, L.-T. Xiao, and S.-T. Jia, Chin. Phys. Lett. **28**, 083701 (2011).

[27] J. Yuan, Z. Ji, Z. Li, Y. Zhao, L. Xiao, and S. Jia, J. Chem. Phys. **143**, 044311 (2015).

[28] D. Su, T. Gong, Z. Ji, Y. Zhao, L. Xiao, S. Jia, C. Li, and J. Liu, Phys. Rev. A **99**, 042513 (2019).

[29] C. Gabbanini and O. Dulieu, Phys. Chem. Chem. Phys. **13**, 18905 (2011).

[30] C. Bruzewicz, M. Gustavsson, T. Shimasaki, and D. DeMille, New J. Phys. **16**, 023018 (2014).

[31] Y.-T. Zhao, J.-P. Yuan, Z.-H. Li, Z.-H. Ji, L.-T. Xiao, and S.-T. Jia, Chin. Phys. Lett. **32**, 113301 (2015).

[32] Z.-H. Ji, Z.-H. Li, T. Gong, Y.-T. Zhao, L.-T. Xiao, and S.-T. Jia, Chin. Phys. Lett. **34**, 103301 (2017).

[33] Z. Ji, H. Zhang, J. Wu, J. Yuan, Y. Yang, Y. Zhao, J. Ma, L. Wang, L. Xiao, and S. Jia, Phys. Rev. A **85**, 013401 (2012).

[34] A. Fioretti and C. Gabbanini, Phys. Rev. A **87**, 054701 (2013).

[35] J. Yuan, Y. Zhao, Z. Ji, Z. Li, J.-T. Kim, L. Xiao, and S. Jia, J. Chem. Phys. **143**, 224312 (2015).

[36] Y. Zhao, J. Yuan, Z. Ji, C. Li, Z. Li, L. Xiao, and S. Jia, J. Quant. Spectrosc. Radiat. Transfer **184**, 8 (2016).

[37] T. Shimasaki, J.-T. Kim, and D. DeMille, ChemPhysChem **17**, 3677 (2016).

[38] Z. Zhang, Z. Ji, Z. Li, J. Yuan, Y. Zhao, L. Xiao, and S. Jia, Chin. Opt. Lett. **13**, 110201 (2015).

[39] Z. Ji, T. Gong, Y. Zhao, C. Li, L. Xiao, and S. Jia, J. Quant. Spectrosc. Radiat. Transfer **254**, 107215 (2020).

[40] H. Katô, Bull. Chem. Soc. Jpn. **66**, 3203 (1993).

[41] E. Arimondo, M. Inguscio, and P. Violino, Rev. Mod. Phys. **49**, 31 (1977).

[42] K. Ishikawa, T. Kumauchi, M. Baba, and H. Katô, J. Chem. Phys. **96**, 6423 (1992).

[43] J. K. G. Watson, J. Mol. Spectrosc. **252**, 5 (2008).

[44] M. Semczuk, X. Li, W. Gunton, M. Haw, N. S. Dattani, J. Witz, A. K. Mills, D. J. Jones, and K. W. Madison, Phys. Rev. A **87**, 052505 (2013).

[45] B. Drews, M. Deiß, J. Wolf, E. Tiemann, and J. Hecker Denschlag, Phys. Rev. A **95**, 062507 (2017).

[46] S. S. Onishchenko, V. B. Sovkov, F. Xie, D. Li, S. S. Lukashov, V. V. Baturo, J. Wu, J. Ma, and L. Li, J. Quant. Spectrosc. Radiat. Transfer **250**, 107037 (2020).

[47] H. Fahs, A. R. Allouche, M. Korek, and M. Aubert-Frécon, J. Phys. B: At., Mol. Opt. Phys. **35**, 1501 (2002).

[48] Y. Lee, Y. Yoon, S. Lee, J.-T. Kim, and B. Kim, J. Phys. Chem. A **112**, 7214 (2008).

[49] I. S. Lim, W. C. Lee, Y. S. Lee, and G.-H. Jeung, J. Chem. Phys. **124**, 234307 (2006).

[50] H. Lefebvre-Brion and R. W. Field, *The Spectra and Dynamics of Diatomic Molecules* (Academic Press, 2004).

[51] J. Aldegunde, B. A. Rivington, P. S. Żuchowski, and J. M. Hutson, Phys. Rev. A **78**, 033434 (2008).

[52] J. Aldegunde and J. M. Hutson, Phys. Rev. A **79**, 013401 (2009).

[53] J. Aldegunde and J. M. Hutson, Phys. Rev. A **96**, 042506 (2017).

[54] J. Aldegunde and J. M. Hutson, Phys. Rev. A **97**, 042505 (2018).

[55] A. V. Oleynichenko, L. V. Skripnikov, A. Zaitsevskii, E. Eliav, and V. M. Shabaev, Chem. Phys. Lett. **756**, 137825 (2020).

[56] P. D. Gregory, J. Aldegunde, J. M. Hutson, and S. L. Cornish, Phys. Rev. A **94**, 041403 (2016).

[57] M. Hughes, M. D. Frye, R. Sawant, G. Bhole, J. A. Jones, S. L. Cornish, M. R. Tarbutt, J. M. Hutson, D. Jaksch, and J. Mur-Petit, Phys. Rev. A **101**, 062308 (2020).

[58] P. D. Gregory, J. A. Blackmore, J. Aldegunde, J. M. Hutson, and S. L. Cornish, Phys. Rev. A **96**, 021402 (2017).

[59] A. Das, P. D. Gregory, T. Takekoshi, L. Fernley, M. Landini, J. M. Hutson, S. L. Cornish, and H.-C. Nägerl, SciPost Phys. **15**, 220 (2023).

[60] R. J. Le Roy, J. Quant. Spectrosc. Radiat. Transfer **186**, 158 (2017).

[61] P. Kowalczyk, J. Chem. Phys. **91**, 2779 (1989).

[62] K. Matsubara, Y.-C. Wang, K. Ishikawa, M. Baba, A. J. McCaffery, and H. Katô, J. Chem. Phys. **99**, 5036 (1993).

[63] K. Ishikawa, J. Chem. Phys. **98**, 1916 (1993).

24 April 2024 12:26:35